EES Solar

PAPER

View Article Online
View Journal | View Issue

Cite this: *EES Sol.*, 2025, **1**, 345

Barrier layer design reduces top electrode ion migration in perovskite solar cells†

Saivineeth Penukula, [a] Megh N. Khanal,[b] Mohin Sharma, [c] Mritunjaya Parashar, [c] Ross A. Kerner, [d] Min Chen,[d] Melissa A. Davis,[d] Rafikul Ali Saha,[e] Eduardo Solano, [f] Maarten B. J. Roeffaers, [e] Joseph J. Berry,[dgh] Joseph M. Luther, [dh] Julian A. Steele, [ij] Axel Palmstrom,[d] Vincent R. Whiteside,[b] Bibhudutta Rout, [c] Ian R. Sellers[b] and Nicholas Rolston *[a]

We report on an examination of mobile ion concentration (N_0) in perovskite solar cells (PSCs) as a function of temperature and device architecture. We find that lower initial N_0 is correlated to devices with higher thermal performance through *in situ* measurements up to 450 K. Changes in N_0 are observed upon thermal aging and are impacted by the changes made at the electron collecting interface. We examine the extent to which various top electrode materials (Ag, Au, carbon) impact N_0 as well as the effects of tin oxide (SnO_2) or an ozone-nucleated SnO_2 (O_3–SnO_2) barrier layer between the ETL and top electrode. Upon thermal aging, we confirm the involvement of Ag ion diffusion through the ETL dependent on the device details. We are able to quantify the degree to which Ag ions migrate or are blocked from migrating into the underlying device layers in the PSC stack. X-ray scattering shows improved suppression of the degradation products formed in the bulk of the perovskite when a blocking layer, particularly the O_3–SnO_2 is employed.

Received 4th April 2025
Accepted 28th April 2025

DOI: 10.1039/d5el00051c

rsc.li/EESSolar

Broader context

Ion migration is one of the important factors that affect the operational lifetime and stability of perovskite solar cells (PSCs). Even though different methodologies have been employed to show the effects of ion migration, the techniques are varied and often qualitative. Furthermore, there is no simple, quantitative method that provides a consistent correlation to the stability of PSCs. This work shows that mobile ion concentration (N_0) can be correlated to PSC stability in state-of-the-art devices. N_0 is a metric that can serve as a consistent and straightforward approach to quantify ion migration-related degradation modes on PSC stability.

Introduction

Metal-halide perovskite (MHP) solar cells have achieved significant commercial interest in the renewable energy market based on rapid efficiency improvements[1,2] achieving lab efficiencies of 26.7%.[3] Additional advantages include the use of earth-abundant precursors, affordable manufacturing, and tunability of optoelectronic properties.[4–7] However, the ion migration and chemical reactions observed under the influence of environmental stressors such as heat and light are a concern.[8,9] The pace of perovskite solar cell (PSC) advances has made it difficult for field testing studies to keep pace with reports in excess of 10 000 h limited to older devices and architectures.[10] Limited field lifetimes (<1 year) for the majority of PSC modules tested by the perovskite PV accelerator for commercializing technologies (PACT)[11] indicates this challenge of demonstrating sufficient reliability to bring PSCs to market. This rapid development cycle creates a need for more rapid testing methods and metrics as well as mechanistic insight

[a]*Renewable Energy Materials and Devices Lab, School of Electrical, Computer and Energy Engineering (ECEE), Arizona State University, Tempe, Arizona 85281, USA. E-mail: nicholas.rolston@asu.edu*

[b]*Department of Electrical Engineering, University at Buffalo SUNY, Buffalo, 230 Davis Hall, New York 14260, USA*

[c]*Department of Physics, Ion Beam Laboratory, University of North Texas, Denton, Texas 76203, USA*

[d]*National Renewable Energy Laboratory, Golden, Colorado 80401, USA*

[e]*cMACS, Department of Microbial and Molecular Systems, KU Leuven, Celestijnenlaan 200F, 3001 Heverlee, Belgium*

[f]*NCD-SWEET Beamline, ALBA Synchrotron Light Source, 08290 Cerdanyola del Vallès, Barcelona, Spain*

[g]*Department of Physics, University of Colorado Boulder, Boulder, Colorado 80309, USA*

[h]*Renewable and Sustainable Energy Institute, University of Colorado Boulder, Boulder, Colorado 80309, USA*

[i]*Australian Institute of Bioengineering and Nanotechnology, The University of Queensland, St Lucia, QLD 4072, Australia*

[j]*School of Mathematics and Physics, The University of Queensland, Brisbane, QLD 4072, Australia*

† Electronic supplementary information (ESI) available. See DOI: https://doi.org/10.1039/d5el00051c

related to stability and reliability issues in PSCs. Of the variety of mechanisms believed to be responsible for a change in efficiency in operation, ion migration is postulated to be a primary cause of this degradation *via* phase separation and reactions with charge transport layers. While these correlations have been identified, the mechanism that ultimately leads to electronic losses and irreversible corrosion of electrodes is still being revealed.[12–15] Here we undertake studies to examine changes in mobile species and how these relate to device stability. Specifically, we use our previously reported measurement approach to study the change in mobile ion concentration (N_0). These measurements are sensitive to mobile charges induced directly or indirectly by mobile ions and chemical reactions, providing a basis from which to see how this changes as devices are stressed, and subsequently examine the specific origins of degradation for a given device architecture.

Recent work has shown that the top metal electrodes in PSCs spontaneously react[15] or can react under electrochemical[16,17] or photochemical stress.[18] One strategy to prevent reactions and the formation of mobile ions is to employ a physical barrier layer.[19] However, this barrier layer must be of very high quality (*i.e.* chemically stable and pinhole-free) to be effective. The best barrier layers are often created by atomic layer deposition (ALD) of metal oxides such as SnO_2 on top of the fullerene-based electron transport layer (ETL) in the p-i-n structure of PSCs.[20] The barrier properties of ALD oxides are further enhanced by ozone-nucleation (O_3) of the SnO_2 by exposing the C_{60} layer to ozone through an ultrathin (~5 nm) non-conformally grown SnO_2 which functionalizes C_{60} to better nucleate subsequent ALD growth and enable more robust internal barriers in PSCs that can prevent chemical reactions and block the motion of ions, water vapor, and solvents.[20] The deposition of the ozone-nucleated barrier layers does not induce any new degradation modes observed under light and heat testing with T_{90} lifetimes of 500 h and 575 h for PSCs with SnO_2 and O_3–SnO_2 layers, respectively, at 65 °C under approximately 1-sun illumination and quasi-maximum power point (quasi-MPP) set by a static load resistor (ISOS-L2-2I).[20] Furthermore, this O_3 nucleation approach was also shown to reduce the water-vapor transmission rate through the barrier layer and reduce gas, solvent, and halide migration, in turn enhancing PSC stability compared to control devices[20] as well as the mechanical robustness of PSCs compared to SnO_2.[21]

Previous work demonstrated that ion migration in PSCs can be quantified in terms of N_0, which is defined as the number of mobile ions present in the MHP, whereby a significant variation in N_0 (5 orders of magnitude) was observed across different samples depending on the composition and chemistry of the top electrode.[22] The reasons for the variation were not well understood at the time. Here, we leverage additional characterization such as Rutherford Backscattering Spectrometry (RBS), a powerful, fast, and non-destructive technique for quantifying elemental motion throughout a PSC. Previous work employed RBS to quantify the depth profile of Pb and I in a film stack comprising TiO_2/$MAPbI_3$.[23] More recently, RBS has been utilized to study the radiation hardness and elemental migration, where the RBS results clearly showed the signs of elemental migration of species such as iodine diffusing from the perovskite to the top electrode.[24] In this work, RBS is used to demonstrate that the migration of Ag ions (and of iodine out of the MHP) can be largely mitigated with a thin ALD SnO_2 barrier layer between the C_{60} layer and the top Ag electrode. This work also elaborates on several other considerations and implications of N_0 that connect to material and device stability, including PSC thermal stability and bulk structural stability.

Results and discussion

Impact of top electrode chemistry on ion migration

We begin by testing our hypothesis that metal electrodes are contributing/impacting N_0 in PSCs with p-i-n architectures by the diffusion of metal ions into the active layer over time or under the influence of environmental stressors such as heat, and that this diffusion can be blocked by barrier layers. N_0 measurements of PSCs with and without barrier layers between the device stack and the top electrode were performed using a transient dark current measurement.[22] The control PSC device stack was glass-ITO/NiO_x/$Cs_{0.2}FA_{0.8}PbI_3$/C_{60}/(Ag or Au or C), as shown in Fig. 1a. A SnO_2 layer was introduced for the SnO_2 PSC and O_3–SnO_2 PSC between the C_{60} ETL and the top electrode (Ag or Au or C) (Fig. 1b and c) deposited on the same substrate to reduce potential variability from different MHP morphologies/microstructures.

Starting with the Ag electrode case, from the square data points in Fig. 1d, the N_0 of the Ag-control PSC was 3.0×10^{14} cm^{-3}. The introduction of barrier layers results in a decreased N_0 value of 1.0×10^{13} cm^{-3} for the Ag–SnO_2 PSC and 1.2×10^{13} cm^{-3} for the Ag–O_3–SnO_2 PSC. We hypothesize that the more than 10× increase in N_0 for the control PSC is due to the diffusion of mobile Ag ions into the MHP lattice through the C_{60} layer. By contrast, when the denser SnO_2 barrier layers (both SnO_2 and O_3 nucleated SnO_2) were used in the device stack, the diffusion of Ag ions was more effectively blocked. This phenomenon has been validated using other characterization methods where diffusion barriers were employed in the device stack to prevent the diffusion and corrosion of the top electrode.[25–27] In this work, the reduction in ion migration is evident by the reduction of N_0 values to a magnitude similar to that of the N_0 values of the considerably more inert Au top electrode both in the case of SnO_2 PSC and O_3–SnO_2 PSC. As such, all 3 device configurations exhibited similar N_0 values for the Au electrode of ~1.7×10^{13} cm^{-3}, whereas the control PSC with C top electrode had a N_0 of 6.7×10^{11} cm^{-3} and both the device configurations with barrier layers and C top electrode had a N_0 of 3×10^{12} cm^{-3}. The slightly reduced value of N_0 in the control PSC when compared to the SnO_2 PSC and O_3–SnO_2 PSC with the C electrode is potentially explained due to two factors. The first is the inertness and chemical stability of C electrodes. The second is the possibility of the C electrode improving the MHP/C_{60} interface through mechanical toughening an effect that we have previously demonstrated from interfacial fracture energy measurements[28] which results in a more physically dense barrier that possibly suppresses the formation of halide vacancies.[29]

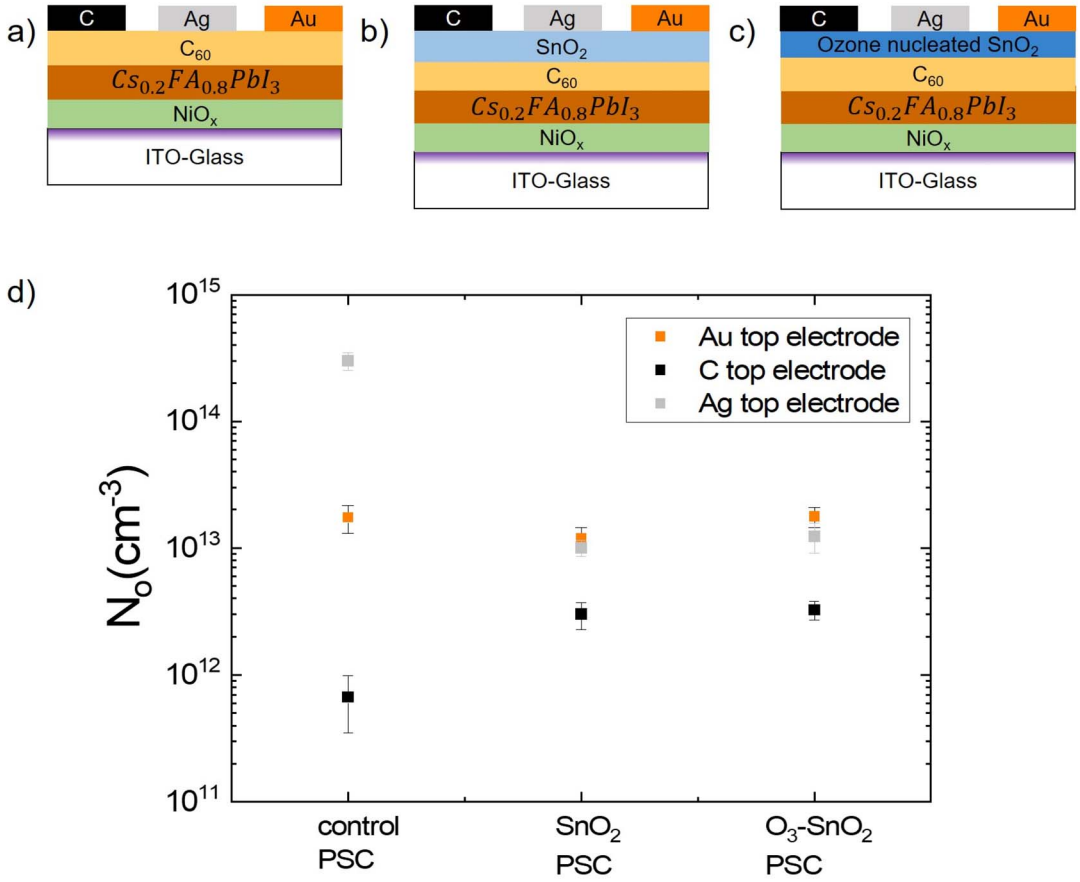

Fig. 1 Impact of top electrode chemistry on ion migration (a) control PSC device stack structure in p-i-n configuration with Ag, Au, and C top electrode on the same substrate. (b and c) Device stack structure of PSCs with a barrier layer between the ETL and top electrode where (b) is the SnO_2 PSC with SnO_2 barrier layer and (c) is the O_3–SnO_2 PSC with ozone nucleated SnO_2 barrier layer. (d) Initial N_0 measurements for control PSC, SnO_2 PSC, and O_3–SnO_2 PSC with Ag, Au, and C top electrodes.

Effectiveness of SnO_2 barrier layer in the prevention of Ag ion diffusion

In addition to the initial N_0, we measured ion evolution under elevated temperatures to study the extent to which additional ion diffusion occurs in the MHP layer. Aging was performed on the PSCs by subjecting them to 50 °C for a period of 120 h. The percentage change in N_0 for all 3 PSC device configurations with respect to the 3 top electrodes was observed after aging (Fig. S1–S3†). The Ag–SnO_2 and Ag–O_3–SnO_2 PSCs had an increase of approximately 740 ± 335% and 90 ± 46% in N_0, respectively, while the N_0 of the Ag-control PSC decreased by 35 ± 9% (Fig. 2a). The N_0 value is believed to be a result of the combination of opposing effects from Ag species reacting with the MHP to generate additional mobile ions and halide ions escaping the MHP lattice to reduce mobile ions after mild thermal aging. This can be seen by the reduction of N_0 measured after thermal aging in the control sample without a SnO_2 barrier layer an effect we attribute to halide ions escaping the MHP lattice and triggering chemical reactions with adjacent layers along with decomposition of the MHP in the bulk, an effect which is shown in Fig. 4. However, we believe that in the case of Ag–SnO_2 and Ag–O_3–SnO_2 PSC where a barrier layer is present, the measured increase in N_0 after aging is primarily a result of metal diffusion into the MHP. In absolute terms, the measured N_0 for aged Ag-control PSCs was still markedly higher than the N_0 of aged Ag–SnO_2 and Ag–O_3–SnO_2 PSCs. After aging, no significant changes in N_0 were observed for PSCs with Au and C top electrodes. A relatively minor decrease (<50% Δ N_0) is one that we previously observed in MHPs with C electrodes. We hypothesize that the mechanism for the minor decrease is due to the possible onset of film degradation based on a slight redshift in photoluminescence after aging under these conditions,[28] which could correspond with mobile ions escaping the MHP lattice.

The above observations strongly indicate that mobile Ag species and MHP-Ag reactions are responsible for the changes in N_0. To probe the redistribution of elements in the devices and confirm the observations, RBS was performed on Ag devices for unaged samples and for thermally aged samples that were subjected to the same thermal aging (50 °C for 120 h) (Fig. S4–S6 and Table S1–S6†). Subsequently, the atomic concentration of elements in all the layers of the device stack was used to understand the roles of Ag and barrier layers affecting ion diffusion in PSCs. Fig. 2b depicts the atomic concentration of Ag

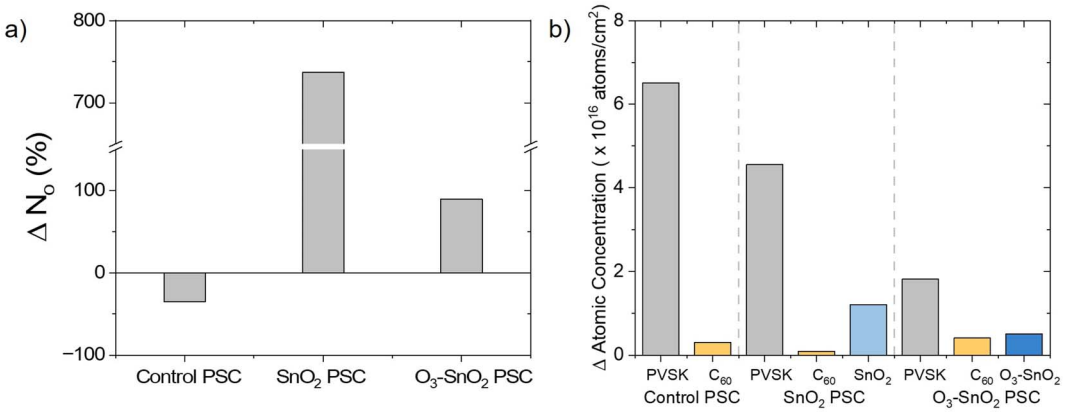

Fig. 2 Effectiveness of SnO_2 barrier layer in the prevention of Ag ion diffusion (a) percentage change in N_0 for control PSC, SnO_2 PSC, and O_3–SnO_2 PSC with Ag top electrodes after exposure of the PSCs to 50 °C for 120 h. (b) Change in RBS atomic concentration of Ag after aging in the MHP layer and ETL for control PSC, along with barrier layer for SnO_2 PSC, and O_3–SnO_2 PSC.

in the MHP layer and other PSC layers (C_{60} layer for Ag-control PSC, C_{60} and SnO_2 layer for Ag–SnO_2 PSC, and C_{60} and O_3–SnO_2 layer for Ag–O_3–SnO_2 PSC) between the MHP and the top electrode for both unaged and aged samples. Note the unaged and aged sample measurements were not performed on the exact same sample before and after aging, which could lead to minor discrepancies in the absolute numbers between samples. There was no significant change in the atomic concentration of Ag in the ETL layers before and after aging with a maximum increase in the atomic concentration of $\sim 0.5 \times 10^{16}$ atoms per cm^2 (Fig. 2b) with the amount of uncertainty as explained in ESI Note 1.† However, a significant increase in the atomic concentration of Ag in the MHP layer was found based on model fitting for all PSCs after aging with almost an eight-fold increase for Ag-control PSC from 1.0×10^{16} to 7.5×10^{16} atoms per cm^2, approximately a four-fold increase for Ag–SnO_2 PSC from 1.4×10^{16} to 6.0×10^{16} atoms per cm^2, and approximately a two-fold increase for Ag–O_3–SnO_2 PSC from 1.2×10^{16} to 3.0×10^{16} atoms per cm^2. Additionally, even though the atomic concentration of Ag increased in the Ag-control PSC after aging, the atomic concentration of iodine is simultaneously reduced (Fig. S7†) in the MHP layer. As previously discussed, these opposing effects on N_0 likely lead to the overall reduction in N_0 observed in Fig. 2a. The increase in the atomic concentration of Ag in the MHP layer for all 3 device configurations after aging confirms that the MHP is reacting with Ag without a SnO_2 barrier layer, and Ag ions are diffusing into the MHP layer over time. It is also clear that O_3–SnO_2 PSC is most effective in reducing the diffusion of Ag into the MHP. The RBS data also shows that no iodine is evident in the layers above the MHP after aging in either the SnO_2 or O_3–SnO_2 device configurations (Tables S4 and S6†), a further indication of the mechanism for N_0 increase in both of those cases being in part due to Ag diffusion into the MHP and doping the material.

Threshold in N_0 for operation and improved thermal stability of PSCs with barrier layer

Accelerated thermal stability tests in the form of *in situ* N_0-temperature measurements were performed for Ag devices, to evaluate the correlation between ion migration and thermal stability. The *in situ* N_0 measurements were undertaken from 300 K to 450 K with a temperature ramp rate of 10 K min^{-1}, a tolerance of 0.5 K, and a settling time of 20 s. We note that thermal tests in the dark were selected to directly probe metal diffusion rather than other forms of instability that arise with heat + light.

The point at which no electronic or ionic response was observed in the device was determined and this threshold temperature was assessed for the different architectures. We note that the apparent threshold temperatures may be either kinetic or thermodynamic effects associated with this temperature ramp experiment. The details of the kinetics of the migration are beyond the current scope of this work. Here, the HTL was either a self-assembled monolayer (SAM) (SAM-based PSC with the control architecture) or NiO_x layer (control, SnO_2, and O_3–SnO_2 PSCs) (Fig. 3a and b). A SAM-based PSC was selected as all state-of-the-art device architectures utilize SAM as the HTL and to demonstrate the versatility of the technique in measuring different device stack structures. From Fig. 3c, the SAM-based PSC and control PSC showed a threshold temperature of 370 K (~100 °C), and the PSCs with barrier layers continued to operate with some response at a temperature of 450 K (~180 °C), the upper limit which was tested for this study. Fig. S8† shows device failure for the control PSC with a loss in dark IV response beyond 370 K and the SAM-based PSC showing a deteriorated dark IV response at 370 K. In comparison, the SnO_2 PSC showed an acceptable dark IV response at 450 K while the O_3–SnO_2 PSC showed an onset of degradation at 440 K, but both the PSCs still had measurable N_0 values at 450 K. It is still expected that this is close to the threshold temperature for their ionic response based on the worsening of the IV curves. This effect was validated by testing a second set of samples with a similar top contact configuration in Fig. S9 and S10,† in which case the O_3–SnO_2 PSCs had an improved thermal stability response compared to both the control and SnO_2 PSCs. In this case, N_0 values for the control were measurable up to 450 K, although the *J–V* response exhibited similar degradation at 370 K and above. We note that a BCP layer was also included in this

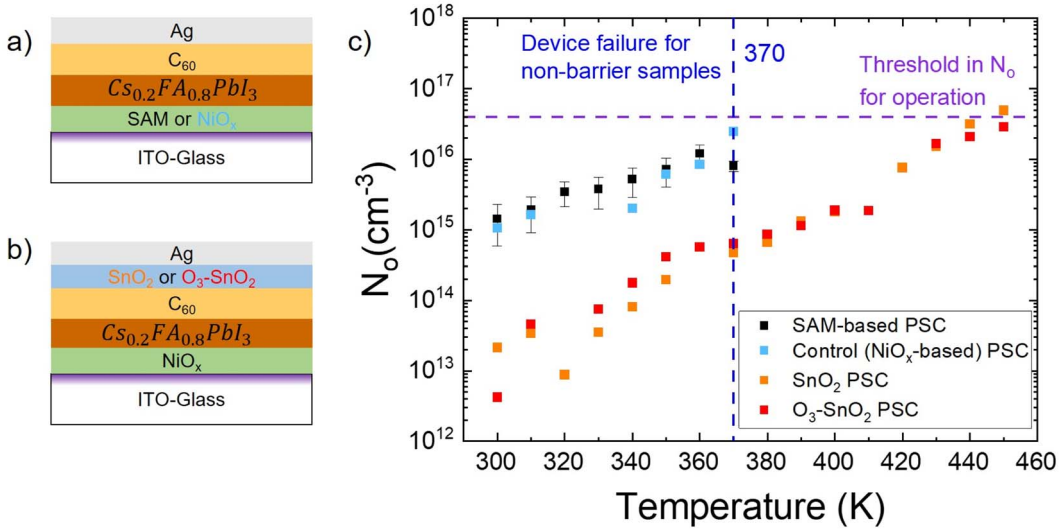

Fig. 3 Threshold in N_0 for operation and improved thermal stability of PSCs with barrier layer (a) device stack structure in p-i-n configuration for control and SAM-based PSC with an HTL of NiO_x and SAM respectively. (b) Device stack structure in p-i-n configuration for SnO_2 PSC and O_3–SnO_2 PSC with a barrier layer of SnO_2 and O_3–SnO_2 respectively between ETL and the top electrode. (c) N_0 of PSCs *versus* temperature, showing threshold operating points of the devices at higher temperatures and also the threshold in N_0 for operation.

batch, and additional N_0 measurements for control devices that contain the BCP aged at 50 °C are included in Fig. S11,† where the PSCs with BCP exhibited a trend in N_0 that is very similar to control PSCs without BCP. This indicates that the introduction of barrier layers in the device stack increased the threshold operating temperature of the PSCs by at least 80 °C, allowing an unencapsulated PSC in this work to function with an Ag electrode at a temperature comparable to the state-of-the-art achieved by a metal-free top contact structure using a combination of ITO with an ALD-based nanolaminate on top of the PSC for additional extrinsic stability shown elsewhere.[30]

Interestingly, there appears to be an empirically observed upper threshold of N_0 for operation at $\sim 3.0 \times 10^{16}$ cm^{-3} for multiple different combinations of electron and hole-transporting layers with Ag contacts, as indicated by the purple dashed line in Fig. 3c above which there is a high possibility of device failure based on the worsening or complete loss of dark IV response for most of the samples as shown in Fig. S8.† All the PSCs showed an increase in N_0 with temperature throughout the temperature range that was tested but the PSCs that had lower N_0 initially (SnO_2 PSC and O_3–SnO_2 PSC) were operational at higher temperatures (370 K to 450 K) when compared to the PSCs that had higher N_0 initially (control PSC and SAM-based PSC) which failed to show a response beyond 370 K. There are multiple interpretations of this observation, all of which are in line with higher N_0 values corresponding to accelerated degradation. One possible mechanism for this observation could be due to other failure modes unrelated to metal diffusion, such as reactions at the HTL/perovskite interface. This shows that having a higher N_0 initially is consistent with more rapid deterioration of PSCs at higher temperatures and that having a lower initial N_0 appears to be one of the factors that are associated with improved thermal stability of these p-i-n PSCs. As such, there is the possibility of implementing N_0 as a screening tool or quality control for validating barrier layer efficacy in PSCs after fabrication.

Improved bulk MHP stability of PSCs with barrier layer

To study how the changes in ions correlate to microstructure changes in the films, GIWAXS was performed on control, SnO_2, and O_3–SnO_2 PSCs before and after the PSCs were subjected to the same thermal aging (50 °C for 120 h in N_2). Incident angle scans showcasing the X-ray diffraction plots in q-space at incidence angles 0.3° (representing the top surface) and 5° (representing the bulk) for all 3 device configurations before and after aging are shown in Fig. 4. Note that the unaged and aged sample measurements were not performed on the same sample. The peaks that indicate some presence of the degradation products were evident on the MHP surface for all the PSCs before and after aging was performed. All the unaged PSCs (Fig. 4a–c) showcased a clear MHP (110) peak in the bulk.[31] However, after aging, the control PSC (Fig. 4d) exhibited a significant diminishing of the MHP (110) peak in the bulk. Note that a slightly higher amount of degradation was observed on the surface in the SnO_2 PSC (Fig. 4e) when compared to the O_3–SnO_2 PSC (Fig. 4f) after aging. Both SnO_2 PSC and O_3–SnO_2 PSC did not show a significant variation in the bulk 1D profile after aging *i.e.*, they retained their MHP (110) peak along with no presence of degradation byproduct peaks. The integrated peak area ratios of MHP (110) and a degradation product (which we hypothesize corresponds to either 2H-$FAPbI_3$ or a non-perovskite phase) (Table S7†) from the 1D integrated GIWAXS profiles show that this ratio reduced from unaged to aged samples in the decreasing order of control PSC, SnO_2 PSC, and O_3–SnO_2 PSC. This reduction indicates that the control PSC has low stability both in the top surface and the bulk, whereas SnO_2 PSCs and O_3–SnO_2 PSCs show an improvement in bulk stability

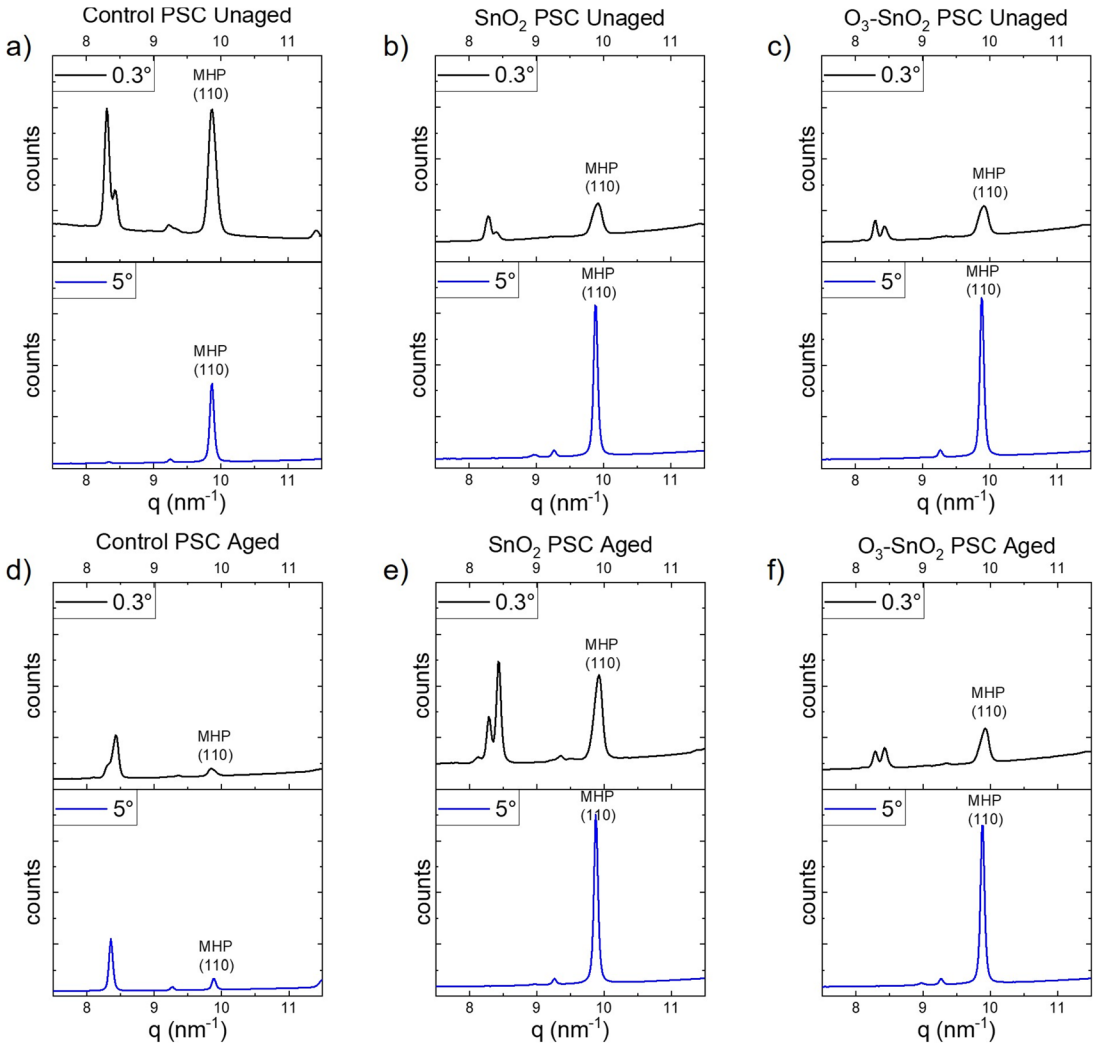

Fig. 4 Improved bulk MHP stability of PSCs with barrier layer X-ray diffraction plots in q-space at incidence angles 0.3° (representing the top surface) and 5° (representing the bulk) (a–c) unaged PSCs, and (d–f) PSCs subjected to 50 °C for 120 h. (a and d) Control PSC, (b and e) SnO_2 PSC, and (c and f) O_3–SnO_2 PSC.

after the introduction of the barrier layers in the device structure.

In addition to the dark I–V measurements, a full set of measurements were performed in the light and complemented by temperature-dependent EQE for the O_3–SnO_2 PSC (showing a minor increase in bandgap with temperature as in line with previous reporting for PSCs with similar compositions[32]) as shown in Fig. S12 and S13.† Control PSCs exhibited a rapid performance degradation with an increase in temperature, whereas O_3–SnO_2 PSCs exhibited much better thermal stability. There was a continuous drop in power conversion efficiency (PCE) from 14.5% to 6.6% for control PSC, whereas the PCE dropped from 16% to 12% for O_3–SnO_2 PSCs when the devices were exposed to heat from 300 K to 450 K. The factors contributing to the drop in PCE of control PSCs are a drop in V_{OC} and fill factor, both of which showed better stability for O_3–SnO_2 PSCs. Hence the improvement in N_0 and the associated enhancement in the O_3–SnO_2 PSCs in comparison to control PSCs is complemented by better stability under extreme operational conditions (Fig. S14†) and is on par with the best reported thermal stability of PSCs, which required the use of a metal-free top contact structure comprising ITO and an ALD nanolaminate[30] on top of the completed device. Our device structure shows that the reactions from a highly reactive metal (Ag) can be mitigated by preventing ion diffusion through the use of an ultra-thin, dense, and well-designed built-in barrier layer.

The activation energy (E_A) of the PSCs was also determined using *in situ* ionic conductivity across a range of temperatures, a measurement that has been used in several other reports for ion-specific activation mechanisms.[33–35] As plotted in Fig. S15 and S16,† the E_A of the control PSC was 0.346 eV, the E_A of the SAM-based PSC was 0.410 eV, and the E_A of the O_3–SnO_2 PSC was 0.503 eV. This value is much higher than the E_A of triple halide PSCs with a similar architecture to the control PSC in this study and without any barrier layer (0.14 eV) from previous

work.[22] As expected, these values support that the mobile ion activation is suppressed in the PSCs with a barrier layer when compared to the control and SAM-based PSCs. The implication of a higher E_A in the O_3–SnO_2 PSC demonstrates that well-designed barrier layers can reduce both the formation and evolution of mobile ions under operational conditions.

The primary focus of this work was utilizing the ion blocking feature/mechanism of a dense ALD O_3–SnO_2 layer to clearly show the diffusion of metal into the MHP under operation and the ability to detect this diffusion using N_0. A mild temperature of 50 °C was initially selected for the exposure tests to be able to observe only the temperature-dependent diffusion mechanisms on the PSCs without the influence of more rapid MHP degradation that could happen if the accelerated testing was done at higher temperatures or with light. Once an understanding regarding the diffusion of metal was achieved at 50 °C, the PSCs were exposed to much higher temperatures up to 450 K (177 °C) to observe the effects of degradation of MHP along with the diffusion of metal into the MHP. Additional experiments were performed under illumination during this high-temperature study showing the improved operational stability of O_3–SnO_2 devices compared to control devices (Fig. S12 and S13†) that directly correlate with the reduction in N_0. Future work will include *in situ* PL mapping characterization of the PSCs to monitor compositional changes in the MHP caused by the metal diffusion under operation during thermal aging.

Conclusion

In this work, we quantified mobile ionic species directly or indirectly resulting from chemical reactions. We demonstrated that our N_0 measurement is sensitive to Ag ions diffusing into the MHP lattice of PSCs through the changes in N_0 based on top electrode chemistry and from thermal aging. We validated that O_3–SnO_2 is an improved barrier layer in preventing the diffusion of Ag ions along with retaining the bulk stability of the MHP while improving PSC thermal stability compared to devices without a barrier layer. This allowed us to correlate this N_0 metric to current–voltage (IV) behavior and ion redistribution as measured by Rutherford Backscattering Spectrometry. It is important to note that at high enough temperatures such as 450 K, MHPs will degrade even with barrier layers due to structural degradation, an effect which was observed in the appearance of an upper threshold for N_0 across device types. While many factors contribute to the real lifetime of fielded PV modules, the effectiveness, and reproducibility of barrier layers to prevent ion migration and chemical degradation are among the most critical to tackle for the stability of PSCs. Overall, our results demonstrate that N_0-temperature measurements are a rapid and effective method to characterize barrier layers at perovskite/electrode interfaces and predict the chemical robustness of the full devices.

To this end, there is a need for a deeper understanding of the correlation between power conversion efficiency, ion migration, and stability of PSCs. As such, we believe that the use of N_0 measurements coupled with accelerated thermal and/or light aging can serve as a highly useful tool in quantifying the extent to which multiple sources of ions (whether from the top electrode or from the MHP itself) move throughout the PSC to provide a deeper understanding of ion-based degradation mechanisms.

Methods

The preparation of glass substrates before doing any of the processing on top of the substrate was performed in a step-by-step procedure as follows: indium tin oxide coated glass (ITO-glass) substrates (Xin Yan Technologies) were initially cleaned in an ultrasonic cleaner by submerging them in an industry grade soap solution of Extran (Millipore Sigma) diluted in water in the ratio of 1 : 10 for 10 min. Then, the ITO-glass slides were rinsed under a flow of de-ionized water with a brush to remove the residual soap on top of the substrates. This was followed by ultrasonic cleaning by submerging them in isopropyl alcohol (IPA) (Thermo Scientific) and acetone (Alfa Aesar–99.5%+) separately for 10 min. Finally, they were subjected to a UV ozone treatment for another 15 min.

Nickel–oxide (NiO_x)

A NiO_x sol–gel solution for depositing the hole transport layer (HTL) was prepared by mixing 1 M $NiNO_3$. $(H_2O)_6$ (Sigma Aldrich–99.999% trace metals basis) in 94% ethylene glycol (EG) (Thermo scientific–anhydrous 99.8%) and 6% ethylenediamine (EDA) (Thermo scientific–99%); the vial was then placed in a vortex mixer, and the solution was mixed until it turned a dark blue color.

Self-assembled monolayer

0.5 mg ml^{-1} MeO-2PACz self-assembled monolayer solution dissolved in ethanol was spin-coated on substrates at 3000 rpm for 30 s in a nitrogen glovebox, followed by annealing at 100 °C for 10 min.

Cesium formamidinium lead iodide ($Cs_{0.2}FA_{0.8}PbI_3$)

The MHP precursor solution for $Cs_{0.2}FA_{0.8}PbI_3$ films was prepared by mixing 0.2 mol Cesium Iodide (CsI) (Sigma-Aldrich–99.999% trace metals basis), 0.8 mol Formamidinium Iodide (FAI) (Greatcell Solar Materials), and 1 mol Lead Iodide (PbI_2) (TCI America–99.99% trace metals basis). A 1 M concentration solution was made by mixing 0.0519 gm of CsI, 0.1375 gm of FAI, and 0.461 gm of PbI_2 in a solvent of 4 : 1 Dimethylformamide (DMF) (Sigma-Aldrich–Anhydrous 99.8%) and Dimethyl Sulfoxide (DMSO) (Sigma-Aldrich–Anhydrous ≥ 99.9%) with 800 μL of DMF and 200 μL of DMSO. A vortex mixer was used to mix the solution until the powders were uniformly dissolved and a yellow solution was formed.

Perovskite solar cells (PSCs)

After finishing the substrate preparation process and making the required inks, PSCs were fabricated in a step-by-step process. As the PSCs were in a p-i-n configuration, the HTL (NiO_x/SAM) was first deposited on the cleaned ITO-glass by spin

coating. 50 μL of NiO_x solution was deposited at a speed of 5000 rpm and an acceleration of 2500 rpm s^{-1} for 30 s in a fume hood and then annealed at 315 °C for 1 h. The SAM layer was deposited at a speed of 3000 rpm for 30 s followed by annealing at 100 °C for 10 min. After the HTL was formed, the MHP absorber layer of $Cs_{0.2}FA_{0.8}PbI_3$ was deposited using a spin coating process with anti-solvent quenching. This was done by depositing 100 μL of MHP precursor on the glass and spinning at a speed of 1000 rpm and acceleration of 500 rpm s^{-1} for 10 s, and then the speed was stepped up to 5000 rpm and acceleration of 1500 rpm s^{-1} for 10 s. In the last 3–5 s of the second step, 100 μL of chlorobenzene (anti-solvent) (Sigma-Aldrich–Anhydrous 99.8%) was deposited quickly. Then, the samples were annealed at 150 °C for 10 minutes. The ETL was deposited by evaporating 45 nm of C_{60} on top of the samples in an Angstrom evaporator with a shadow mask, and the top electrode was made by evaporating either 100 nm of Ag or Au on top of the device stack using a different mask. The carbon (C) top electrode was formed on top of the PSC by depositing it from the solvent-based C paste (PELCO conductive carbon glue–Ted Pella). Three different electrodes (evaporated Ag or Au and a solvent-based C) were deposited on top of the same PSC substrate to observe the variation in N_0 with respect to barrier layers and the top electrode. ALD SnO_2 and O_3–SnO_2 for the barrier layers were deposited in a Beneq TFS200 ALD reactor by 125 cycles of tetrakisdimethylamino tin(IV) and water at 90. A 15 second ozone and water treatment was applied to the O_3–SnO_2 samples *in situ* part way through the 125 cycles SnO_2 deposition following the sequence: 40 cycles SnO_2/15 second ozone and water/85 cycle SnO_2.[20]

Characterization

All the ionic and electronic measurements were performed with PAIOS, an all-in-one measurement equipment for photovoltaic devices and LEDs (FLUXiM AG). A hot plate was used to age the PSCs (as fabricated without encapsulation) at 50 °C in an N_2 glovebox for 120 h with *ex situ* measurements on PAIOS. N_0 was measured and calculated using the transient dark current method (Fig. S17†) as described in our previous work[22] in which a voltage bias of 800 mV is applied to the PSC in a forward-bias configuration in the form of a pulse with the following characteristics: 1 ms settling time, 10 ms pulse time, and 1 ms follow-up time. The entire measurement lasts around 13 ms with the measurement cut-off around 1 ms after the bias is taken away, during which the mobile ions in the MHP drift. The measured drift current can be time-integrated and divided by the elementary charge, area, and thickness of the MHP layer respectively to determine the N_0.[22] For the quantification of mobile ion concentration (N_0) using the transient dark current methodology, the voltage pulse is applied in forward bias for only a short time of 10 ms. This timescale was chosen to be able to only measure the intrinsic concentration of ions in the perovskite that are ready to move under a small voltage perturbation. Using such a short timescale for the measurement might result in values of N_0 that are lower than what has been reported in the literature, but we believe that the values obtained represent the actual ionic concentration present in the device at the surface level or at the interfaces. The consistency of the measured N_0 values has been shown in our previous works.[22,28,35]

In situ ionic measurements were performed with the temperature control stage and module (LTS-420E) from Linkam in integration with PAIOS in increments of 10 K from room temperature (300 K) up to 450 K. E_A was measured following the same methodology used in our previous work.[35] The ramp rate used was 10 K min^{-1} and the tolerance was 0.5 K with a settling time of 20 s. The reported E_A values are based on measurements of a single sample. However, the samples were measured during both ramp up and ramp down of the temperature. The reduction of temperature happened naturally and hence the samples would have significant dwell at each temperature and the calculations include averages of the measurement in both directions.

The RBS experiment was conducted in the Ion beam laboratory (IBL) at the University of North Texas (UNT) using the NEC 9SH 3 MV Pelletron accelerator.[36,37] All the experiments were performed in the ion microprobe beamline using a 2 MeV He^+ beam under a vacuum of 2×10^{-7} Torr. The RBS spectra were collected using a Passivated Implanted Planar Silicon (PIPS) charged particle detector from Mirion Technologies (Canberra), model No. PD25-11-300 AM, having a solid angle of 34 milli-steradian, and the operating voltage for the detector was 40 V situated at the backscattered angle of 145° (Fig. S18†). The detector arrangement in the microprobe chamber is such that the incident beam, backscattering detector, and target normal lie in the same horizontal plane.

The RBS data fitting was done using the SIMNRA software package.[38] Based on the thickness values of each layer in the PSC stack, a simulated sample was generated. The concentrations of each layer were adjusted until a suitable match was achieved. Layer thickness is accepted by SIMNRA in the form of the layer's areal density (atoms cm^{-2}). The SRIM/TRIM software program was utilized to convert the thickness into areal density[39] and detailed information on the process is provided elsewhere.[24] The layer information extracted from the SIMNRA was fed into the MultiSIMNRA[40] software program, to further extract the contribution from the individual layers and their elemental species.

To identify the different crystalline phases in the perovskite films and devices, at different subsurface depths, synchrotron-based grazing incidence wide-angle X-ray scattering (GIWAXS) data were collected at NCD-SWEET beamline at the ALBA synchrotron (Cerdanyola del Vallès, Spain): a monochromatic ($\lambda = 0.95741$ Å) X-ray beam of 150×30 μm^2 [$H \times V$] was defined using a Si (111) channel cut monochromator and collimated using Be Compound Refractive Lenses (CRLs). The scattered signal was recorded using a Rayonix LX255-HS area detector placed at 251.2 mm from the sample position. Detector tilts and sample-to-detector distance were calculated using Cr_2O_3 as a calibrant, which was employed to calibrate the reciprocal space wavevector, q. GIWAXS frames were recorded at incident angles (α_i) between 0° and 5° in a scanning fashion, shifting from the surface-sensitive evanescent regime of scattering and

transitioning to a deep penetrative measurement of the film layers at relatively high angles.[41] Throughout the data acquisition process, a continuous flow of N_2 gas was maintained over the sample. Collected 2D images were azimuthally integrated to general 1D profiles using PyFAI[42] and processed using a custom Python routine.

Data availability

The data that support the findings of this study are available from the corresponding author upon reasonable request.

Author contributions

Conceptualization, S. P. and N. R.; methodology, S. P. and N. R.; investigation, S. P., M. N. K., M. S., M. P., M. C., R. A. S., and E. S.; validation S. P. and R. A. K.; formal analysis S. P., M. N. K., M. S., M. P., and J. A. S.; data curation S. P.; visualization S. P. and N. R.; writing–original draft, S. P. and N. R.; writing–review & editing S. P., M. N. K., M. S., M. P., M. A. D., R. A. K., M. C., R. A. S., E. S., M. B. J. R, I. R. S, V. R. W., J. J. B., J. M. L., J. A. S., A. P., B. R., and N. R.; resources S. P., M. C., I. R. S., J. M. L., M. A. D., J. A. S., A. P., and B. R.; visualization S. P. and N. R.; software S. P., M. N. K., M. S., M. P., and J. A. S.; supervision M. B. J. R., I. R. S., V. R. W., J. J. B., J. M. L., J. A. S., A. P., B. R., and N. R.; project administration N. R.; funding acquisition M. B. J. R., J. J. B., J. M. J., J. A. S., A. P., B. R., and N. R.; All the authors discussed the results and commented on the manuscript.

Conflicts of interest

S. P. and N. R. have filed for a patent based on this work. The other authors declare no conflict of interest.

Acknowledgements

This material is based upon work supported by the National Science Foundation under Grant No. 2339233. This work was authored in part by the National Renewable Energy Laboratory for the U.S. Department of Energy (DOE) under Contract No. DE-AC36-08GO28308. A. P., J. J. B., and R. A. K acknowledges financial support from the U.S. Department of Energy's Office of Energy Efficiency and Renewable Energy (EERE) under Solar Energy Technologies Office (SETO) Agreement DE- EE0009513. The views expressed in the article do not necessarily represent the views of the DOE or the U.S. Government. J. A. S acknowledges financial support from the Australian Research Council (ARC: grant no. DE230100173. J. A. S., R. A. S., and M. B. J. R. thank the staff of the BL11 NCD-SWEET beamline for their assistance in recording the synchrotron GIWAXS data. R. A. S. and M. B. J. R. acknowledge financial support from iBOF-21-085 PERsist and Internal Funds KU Leuven (C14/23/090). B. R., M. S., and M. P. acknowledge financial support from the U.S. National Science Foundation Grant No. ECCS-2210722.

References

1 Z. Li, B. Li, X. Wu, S. A. Sheppard, S. Zhang, D. Gao, *et al.*, Organometallic-functionalized interfaces for highly efficient inverted perovskite solar cells, *Science*, 2022, **376**(6591), 416–420, DOI: **10.1126/science.abm8566**.

2 J. J. Yoo, G. Seo, M. R. Chua, T. G. Park, Y. Lu, F. Rotermund, *et al.*, Efficient perovskite solar cells *via* improved carrier management, *Nature*, 2021, **590**(7847), 587–593, DOI: **10.1038/s41586-021-03285-w**.

3 NREL Best Research-Cell Efficiency Chart, 2024, **https://www.nrel.gov/pv/cell-efficiency.html**.

4 M. A. Green, A. Ho-Baillie and H. J. Snaith, The emergence of perovskite solar cells, *Nat. Photonics*, 2014, **8**(7), 506–514, DOI: **10.1038/nphoton.2014.134**.

5 M. Ashif and F. Mahjabeen, Promises and Challenges of Perovskite Solar Cells: A Comprehensive Review, *BULLET: Jurnal Multidisiplin Ilmu*, 2023, **2**(5), 1147–1157. Available from: **https://journal.mediapublikasi.id/index.php/bullet/article/view/3685**.

6 P. Čulík, K. Brooks, C. Momblona, M. Adams, S. Kinge, F. Maréchal, *et al.*, Design and Cost Analysis of 100 MW Perovskite Solar Panel Manufacturing Process in Different Locations, *ACS Energy Lett.*, 2022, **7**(9), 3039–3044, DOI: **10.1021/acsenergylett.2c01728**.

7 R. H. Ahangharnejhad, W. Becker, J. Jones, A. Anctil, Z. Song, A. Phillips, *et al.*, Environmental Impact per Energy Yield for Bifacial Perovskite Solar Cells Outperforms Crystalline Silicon Solar Cells, *Cell Rep. Phys. Sci.*, 2021, **2**(2), 100344. Available from: **https://www.sciencedirect.com/science/article/pii/S2666386421000291**.

8 K. Sakhatskyi, R. A. John, A. Guerrero, S. Tsarev, S. Sabisch, T. Das, *et al.*, Assessing the Drawbacks and Benefits of Ion Migration in Lead Halide Perovskites, *ACS Energy Lett.*, 2022, **7**(10), 3401–3414, DOI: **10.1021/acsenergylett.2c01663**.

9 J. Liu, M. Hu, Z. Dai, W. Que, N. P. Padture and Y. Zhou, Correlations between Electrochemical Ion Migration and Anomalous Device Behaviors in Perovskite Solar Cells, *ACS Energy Lett.*, 2021, **6**(3), 1003–1014, DOI: **10.1021/acsenergylett.0c02662**.

10 G. Grancini, C. Roldán-Carmona, I. Zimmermann, E. Mosconi, X. Lee, D. Martineau, *et al.*, One-Year stable perovskite solar cells by 2D/3D interface engineering, *Nat. Commun.*, 2017, **8**(1), 15684, DOI: **10.1038/ncomms15684**.

11 Perovskite PV Accelerator for Commercializing Technologies. 2024, **https://pvpact.sandia.gov/**.

12 E. Bi, Z. Song, C. Li, Z. Wu and Y. Yan, Mitigating ion migration in perovskite solar cells, *Trends Chem.*, 2021, **3**(7), 575–588, DOI: **10.1016/j.trechm.2021.04.004**.

13 H. Zai, Y. Ma, Q. Chen and H. Zhou, Ion migration in halide perovskite solar cells: Mechanism, characterization, impact and suppression, *J. Energy Chem.*, 2021, **63**, 528–549. Available from: **https://www.sciencedirect.com/science/article/pii/S2095495621004290**.

14 Y. Zhao, W. Zhou, Z. Han, D. Yu and Q. Zhao, Effects of ion migration and improvement strategies for the operational

stability of perovskite solar cells, *Phys. Chem. Chem. Phys.*, 2021, **23**(1), 94–106, DOI: **10.1039/D0CP04418K**.

15 L. Zhao, R. A. Kerner, Z. Xiao, Y. L. Lin, K. M. Lee, J. Schwartz, *et al.*, Redox Chemistry Dominates the Degradation and Decomposition of Metal Halide Perovskite Optoelectronic Devices, *ACS Energy Lett.*, 2016, **1**(3), 595–602, DOI: **10.1021/acsenergylett.6b00320**.

16 R. A. Kerner, L. Zhao, S. P. Harvey, J. J. Berry, J. Schwartz and B. P. Rand, Low Threshold Voltages Electrochemically Drive Gold Migration in Halide Perovskite Devices, *ACS Energy Lett.*, 2020, **5**(11), 3352–3356, DOI: **10.1021/acsenergylett.0c01805**.

17 R. A. Kerner, A. V. Cohen, Z. Xu, A. R. Kirmani, S. Y. Park, S. P. Harvey, *et al.*, Electrochemical Doping of Halide Perovskites by Noble Metal Interstitial Cations, *Adv. Mater.*, 2023, **35**(29), 2302206, DOI: **10.1002/adma.202302206**.

18 N. N. Shlenskaya, N. A. Belich, M. Grätzel, E. A. Goodilin and A. B. Tarasov, Light-induced reactivity of gold and hybrid perovskite as a new possible degradation mechanism in perovskite solar cells, *J. Mater. Chem. A*, 2018, **6**(4), 1780–1786, DOI: **10.1039/C7TA10217H**.

19 J. Zhou, Z. Liu, P. Yu, G. Tong, R. Chen, L. K. Ono, *et al.*, Modulation of perovskite degradation with multiple-barrier for light-heat stable perovskite solar cells, *Nat. Commun.*, 2023, **14**(1), 6120, DOI: **10.1038/s41467-023-41856-9**.

20 S. A. Johnson, K. P. White, J. Tong, S. You, A. Magomedov, B. W. Larson, *et al.*, Improving the barrier properties of tin oxide in metal halide perovskite solar cells using ozone to enhance nucleation, *Joule*, 2023, **7**(12), 2873–2893, DOI: **10.1016/j.joule.2023.10.009**.

21 M. Li, S. Johnson, L. Gil-Escrig, M. Sohmer, C. A. Figueroa Morales, H. Kim, *et al.*, Strategies to improve the mechanical robustness of metal halide perovskite solar cells, *Energy Adv.*, 2024, **3**(1), 273–280, DOI: **10.1039/D3YA00377A**.

22 S. Penukula, R. Estrada Torrejon and N. Rolston, Quantifying and Reducing Ion Migration in Metal Halide Perovskites through Control of Mobile Ions, *Molecules*, 2023, **28**(13), 5026. Available from: **https://www.mdpi.com/1420-3049/28/13/5026**.

23 F. Lang, A. Juma, V. Somsongkul, T. Dittrich and M. Arunchaiya, Rutherford Backscattering Spectroscopy of Mass Transport by Transformation of PbI2 into CH3NH3PbI3 within np-TiO2, *Hybrid. Mater.*, 2014, **1**(1), 52–61.

24 M. Parashar, M. Sharma, D. K. Saini, T. A. Byers, J. M. Luther, I. R. Sellers, *et al.*, Probing elemental diffusion and radiation tolerance of perovskite solar cells *via* non-destructive Rutherford backscattering spectrometry, *Appl. Energy*, 2024, **2**(1), 016109, DOI: **10.1063/5.0193601**.

25 H. H. Park and D. J. Fermin, Recent Developments in Atomic Layer Deposition of Functional Overlayers in Perovskite Solar Cells, *Nanomaterials*, 2023, **13**(24), 3112. Available from: **https://www.mdpi.com/2079-4991/13/24/3112**.

26 E. Bi, H. Chen, F. Xie, Y. Wu, W. Chen, Y. Su, *et al.*, Diffusion engineering of ions and charge carriers for stable efficient perovskite solar cells, *Nat. Commun.*, 2017, **8**(1), 15330, DOI: **10.1038/ncomms15330**.

27 N. Li, Z. Shi, C. Fei, H. Jiao, M. Li, H. Gu, *et al.*, Barrier reinforcement for enhanced perovskite solar cell stability under reverse bias, *Nat. Energy*, 2024, **9**, 1264–1274, DOI: **10.1038/s41560-024-01579-7**.

28 S. Penukula, F. Tippin, M. Li, K. A. Khawaja, F. Yan and N. Rolston, Use of carbon electrodes to reduce mobile ion concentration and improve reliability of metal halide perovskite photovoltaics, *Energy Mater.*, 2024, **4**(5), 400060, DOI: **10.20517/energymater.2024.26**. Available from: **https://www.oaepublish.com/articles/energymater.2024.26**.

29 Y. Zhong, J. Yang, X. Wang, Y. Liu, Q. Cai, L. Tan, *et al.*, Inhibition of Ion Migration for Highly Efficient and Stable Perovskite Solar Cells, *Adv. Mater.*, 2023, **35**(52), 2302552, DOI: **10.1002/adma.202302552**.

30 H. Afshari, S. Sourabh, S. A. Chacon, V. R. Whiteside, R. C. Penner, B. Rout, *et al.*, FACsPb Triple Halide Perovskite Solar Cells with Thermal Operation over 200 °C, *ACS Energy Lett.*, 2023, **8**(5), 2408–2413, DOI: **10.1021/acsenergylett.3c00551**.

31 Y. Yang, L. Yang and S. Feng, Interfacial engineering and film-forming mechanism of perovskite films revealed by synchrotron-based GIXRD at SSRF for high-performance solar cells, *Mater. Today Adv.*, 2020, **6**, 100068. Available from: **https://www.sciencedirect.com/science/article/pii/S2590049820300151**.

32 T. Moot, J. B. Patel, G. McAndrews, E. J. Wolf, D. Morales, I. E. Gould, *et al.*, Temperature Coefficients of Perovskite Photovoltaics for Energy Yield Calculations, *ACS Energy Lett.*, 2021, **6**(5), 2038–2047, DOI: **10.1021/acsenergylett.1c00748**.

33 M. C. López-González, G. del Pozo, B. Arredondo, S. Delgado, D. Martín-Martín, M. García-Pardo, *et al.*, Temperature behaviour of mixed-cation mixed-halide perovskite solar cells. Analysis of recombination mechanisms and ion migration, *Org. Electron.*, 2023, **120**, 106843. Available from: **https://www.sciencedirect.com/science/article/pii/S156611992300099X**.

34 J. Xing, Q. Wang, Q. Dong, Y. Yuan, Y. Fang and J. Huang, Ultrafast ion migration in hybrid perovskite polycrystalline thin films under light and suppression in single crystals, *Phys. Chem. Chem. Phys.*, 2016, **18**(44), 30484–30490, DOI: **10.1039/C6CP06496E**.

35 J. Sun, S. Penukula, M. Li, M. R. Hosseinzade, Y. Tang, L. Dou, *et al.*, Mechanical and Ionic Characterization for Organic Semiconductor-Incorporated Perovskites for Stable 2D/3D Heterostructure Perovskite Solar Cells, *Small*, 2024, 2406928, DOI: **10.1002/smll.202406928**.

36 B. Rout, M. S. Dhoubhadel, P. R. Poudel, V. C. Kummari, B. Pandey, N. T. Deoli, *et al.*, An overview of the facilities, activities, and developments at the University of North Texas Ion Beam Modification and Analysis Laboratory (IBMAL), *AIP Conf. Proc.*, 2013, **1544**(1), 11–18, DOI: **10.1063/1.4813454**.

37 M. Sharma, M. Parashar, D. K. Saini, T. A. Byers, C. Bowen and M. N. Khanal, *et al.*, *In situ* Characterization Tools for

Evaluating Radiation Tolerance and Elemental Migration in Perovskites. in *2024 IEEE 52nd Photovoltaic Specialist Conference (PVSC)*. 2024. pp. 496–498.

38 M. Mayer, *SIMNRA User's Guide*. 1997, **https://mam.home.ipp.mpg.de/ReportIPP9-113.pdf**.

39 J. F. Ziegler, M. D. Ziegler and J. P. Biersack, SRIM – The stopping and range of ions in matter (2010), *Nucl. Instrum. Methods Phys. Res., Sect. B*, 2010, **268**(11), 1818–1823. Available from: **https://www.sciencedirect.com/science/article/pii/S0168583X10001862**.

40 T. F. Silva, C. L. Rodrigues, M. Mayer, M. V. Moro, G. F. Trindade, F. R. Aguirre, *et al.*, MultiSIMNRA: A computational tool for self-consistent ion beam analysis using SIMNRA, *Nucl. Instrum. Methods Phys. Res., Sect. B*, 2016, **371**, 86–89. Available from: **https://www.sciencedirect.com/science/article/pii/S0168583X15010459**.

41 J. A. Steele, E. Solano, D. Hardy, D. Dayton, D. Ladd, K. White, *et al.*, How to GIWAXS: Grazing Incidence Wide Angle X-Ray Scattering Applied to Metal Halide Perovskite Thin Films, *Adv. Energy Mater.*, 2023, **13**(27), 2300760, DOI: **10.1002/aenm.202300760**.

42 G. Ashiotis, A. Deschildre, Z. Nawaz, J. P. Wright, D. Karkoulis, F. E. Picca, *et al.*, The fast azimuthal integration Python library: pyFAI, *J. Appl. Crystallogr.*, 2015, **48**(2), 510–519, DOI: **10.1107/S1600576715004306**.